

3D stereolithography printing of graphene oxide reinforced complex architectures

Dong Lin^{1,2,3}, Shengyu Jin^{1,3}, Feng Zhang⁴, Chao Wang⁵, Yiqian Wang⁵,
Chi Zhou⁴ and Gary J Cheng^{1,6,3}

¹ School of Industrial Engineering, Purdue University, West Lafayette, IN 47906, USA

² Department of Industrial and Manufacturing Systems Engineering, Kansas State University, Manhattan, KS 66506, USA

³ Birck Nanotechnology Center, Purdue University, West Lafayette, IN 47906, USA

⁴ Department of Industrial and Systems Engineering, University at Buffalo, the State University of New York, Buffalo, NY 14260, USA

⁵ The Cultivation Base for State Key Laboratory & College of Physics, Qingdao University, People's Republic of China

⁶ School of Mechanical Engineering, Purdue University, West Lafayette, IN 47906, USA

E-mail: chizhou@buffalo.edu and gjcheng@purdue.edu

Received 13 July 2015, revised 26 August 2015

Accepted for publication 7 September 2015

Published 7 October 2015



CrossMark

Abstract

Properties of polymer based nanocomposites rely on distribution, concentration, geometry and property of nanofillers in polymer matrix. Increasing the concentration of carbon based nanomaterials, such as CNTs, in polymer matrix often results in stronger but more brittle material. Here, we demonstrated the first three-dimensional (3D) printed graphene oxide complex structures by stereolithography with good combination of strength and ductility. With only 0.2% GOs, the tensile strength is increased by 62.2% and elongation increased by 12.8%. Transmission electron microscope results show that the GOs were randomly aligned in the cross section of polymer. We investigated the strengthening mechanism of the 3D printed structure in terms of tensile strength and Young's modulus. It is found that an increase in ductility of the 3D printed nanocomposites is related to increase in crystallinity of GOs reinforced polymer. Compression test of 3D GOs structure reveals the metal-like failure model of GOs nanocomposites.

 Online supplementary data available from stacks.iop.org/NANO/26/434003/mmedia

Keywords: 3D printing, graphene composite, stereolithography

(Some figures may appear in colour only in the online journal)

Introduction

3D printing, more commonly known as additive manufacturing (AM) [1], is a collection of emerging technologies that create three-dimensional (3D) objects from the bottom to top by adding material in a layer by layer basis. Since AM can directly fabricate a product from 3D digital models, it has been widely recognized as a disruptive manufacturing technology for a wide variety of applications and consequently hailed as the third industrial revolution [2]. However, despite tremendous effort and significant progress made in AM, a number of technical challenges still remain. In a recent NSF

workshop [3] on developing the roadmap for AM, the limited material selection has been identified as one of the key barriers and challenges which has to be addressed for current AM processes and machines. The majority of materials used by current AM techniques are polymers, though some metal or ceramic materials are used in some high end machines [4]. The weak mechanical property of the polymer and poor surface quality of the metal parts has severely hindered the further progress of AM technology. Paralleling the development of AM technology during the past decade, significant efforts have also been devoted to the development of polymer nanocomposites. By incorporating nano particles into

polymers, the nanocomposites exhibit significantly improved mechanical, thermal, optical or other properties [5].

On the other hand, graphene, a single layer of sp^2 hybridized carbon atoms forming a 2D hexagonal lattice, has a breaking strength 200 times larger than that of steel and a Young's modulus of 1 TPa [6–8]. It has been applied to improve properties of polymers, including mechanical properties [1, 9–17], electrical properties [18–20], thermal properties [1, 21, 22], optical properties [23, 24], electromagnetic interference shielding [25, 26] and barrier properties [27–29]. The design and behavior of polymer nanocomposites mainly depend on the aspect ratio of nanofillers, percolation threshold and interfacial property of nanofiller and matrix [7]. Dispersion of nanofillers is crucial for the properties of polymer nanocomposites. The mechanism for the interaction in graphene/polymer nanocomposites relies on the polarity, molecular weight, hydrophobicity, reactive groups, etc [20, 30]. Nanocomposites' properties will be maximally reinforced by a well dispersed state [8, 16, 17, 31]. Therefore, large efforts have been focused on achieving a homogeneous and well dispersed graphene/GO in polymer matrix [32]. Three strategies have been applied to prepare graphene/polymer or GO/polymer:

- (a) *In situ* intercalative polymerization. In this method, graphene or GO is first swollen in the liquid monomer, then a suitable initiator is diffused and polymerization reaction proceeds by heat or radiation [30, 32].
- (b) Solution intercalation. Three steps are involved in this method: dispersion of graphene or GO in a suitable solvent, addition of polymer and removal of the solvent [32]. Graphene or GO can be dispersed in various solvents, which can be water, acetone, chloroform, tetrahydrofuran, dimethyl formamide or toluene, by ultrasonication [30, 32]. Graphene or GO sheets are delaminated by breaking the weak forces that stack these layers together, and the polymer then is adsorbed onto these sheets [33]. The separated graphene sheets sandwich the polymer to form a nanocomposite by removing solvent, which is crucial for the properties of nanocomposites [34]. Entropy increase by desorption of solvent molecules is the driving force for polymer intercalation, which compensates the decreasing entropy of intercalating polymer chains [30]. It means large quantity of solvent molecules need for desorbing from graphene or GO sheets to accommodate incoming polymer chains [35]. The main advantage of this method is introducing low or even no polarity during synthesis process.
- (c) Melt intercalation. Graphene or GO is mechanically mixed with thermoplastic polymer at elevated temperatures by extrusion or injection molding [36–38]. Nanocomposites are formed by intercalating or exfoliating polymer chains. This method is solvent free.

Graphene or graphene oxide reinforced polymer composites have been under intensive investigation. Rafiee *et al* revealed the significant fatigue life increase in graphene nanocomposites [10]. Yavari *et al* reported that graphene

reinforced polymer composites have best fatigue life when compared to single wall carbon nanotube composites, multi-wall carbon nanotube composites and glass–fiber/epoxy composites [39]. The ultimate strength of a 1 wt.% functionalized graphene sheet reinforced PMMA increased by 20% [1]. The tensile strength of 0.9 wt.% of graphene reinforced polystyrene (PS) increased by 69.5%. Zhao *et al* investigated the tensile strength of 1.8 vol.% graphene reinforced poly(vinyl alcohol) and observed around 150% increase [13]. Significant improvement (2.2 folds) of tensile strength was achieved by adding 0.1 wt.% of graphene oxide into prepare nylon-6-(PA6-) [15]. However, all the graphene composites had a big loss in ductility.

In this research, we investigated the printing of reinforced photopolymer parts by incorporating the advanced nanofillers (graphene oxide) and the accurate AM process (stereolithography). Nanofillers have been added into photopolymer by the solution intercalation method. Stereolithography processes involved selective curing of pre-deposited photopolymer using some type of light source. Two primary configurations, namely, vector scanning based and mask projection based styles have been commonly used in practice. The vector scanning based system has relatively high precision. Sandoval, *et al* [40, 41] exploited multi-walled carbon nanotubes (MWCNT) reinforced photopolymer in vector scanning based stereolithography. The experimental results show that a small concentration of MWCNTs can result in significant effects on the physical properties of the photopolymer resin. A MWCNT concentration of 0.025% increased the ultimate tensile stress (TS) and fracture stress (FS) on average of 5.7% and 26% respectively. Increasing the MWCNT concentration to 0.1% resulted in increase in TS and FS of 7.5% and 33% respectively. However, the addition of MWCNTs in the resin resulted in a more brittle material. The nanocomposite specimens experienced a decrease in elongation by $\sim 28\%$ compared with the pure resin. In this paper, we report a method to print 3D GOs polymer composite with significant improvement in tensile strength without sacrificing ductility. In addition, a novel fracture phenomenon of 3D printed truss architecture under compression test will be firstly revealed.

Experimental section

Materials

Single-layer graphene oxide (SLGO) was supplied by Cheaptubes Inc. The size range of SLGO at *X*- and *Y*-dimensions is from 300 nm to 10 μm and the thickness range is 0.9 ± 0.2 nm measured by AFM [8, 17].

Dispersion GO in polymer

The expected weight amount of SLGO was dispersed in acetone (100 ml acetone with 0.1 g SLGO) by applying an ultrasonic separation (VWR B1500A-DTH) for 2 h in ice bath [10]. The polymer resin (Pic 100 from EnvisionTEC) was

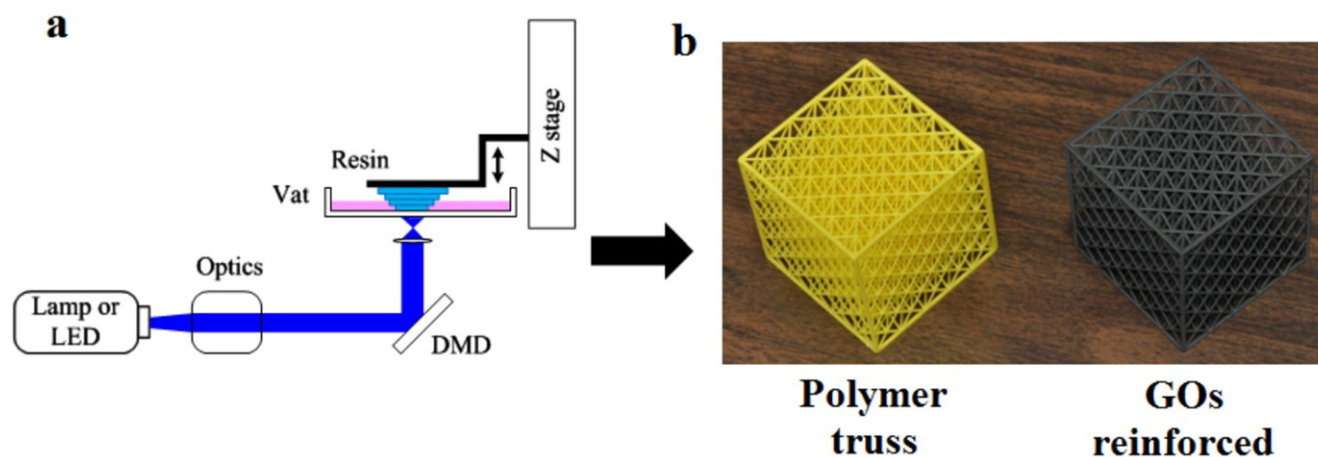


Figure 1. 3D printing of GO-reinforced polymer. (a) Schematic of SLA-based 3D printing process. (b) 3D printed polymer truss part and GO-reinforced polymer truss part.

added to the suspension and sonicated for another 2 h in an ice bath. After that, the acetone was evaporated by heating and stirring by a Teflon-coated magnetic stir for 12 h at 70 °C.

3D printing

In a mask projection based stereolithography (MPSL) system, the light energy of the whole working area can be controlled simultaneously and dynamically. Therefore, compared with the vector scanning process, where only one dot is used as the light source, the MPSL process can be much faster especially for complex shapes [42]. In this study, we investigated a bottom-up MPSL process for tailoring the mechanical properties of photopolymer resin by dispersing controlled amount of graphene. In this process, the 3D digital model of an object is firstly sliced by a set of horizontal planes. Each slice is then converted into a two-dimensional (2D) mask image. The related mask images are then sent to the projection devices such as a digital micromirror device and projected onto a resin surface such that the liquid resin can be selectively cured accordingly to the mask image to form the layer of the object. By repeating the process, 3D objects can be formed on a layer-by-layer basis. As shown in figure 1(a), the bottom-up process projects the image from the bottom of a transparent vat. A super elastic intermediate media is applied at the bottom of the vat in order to facilitate the separation between new cured layer and the vat. Compared with top-down process, bottom-up process provides several advantages associated with the nanocomposite 3D printing process [43]: since the new cured layer is constrained between the previous layer and vat bottom, much smaller layer thickness can be achieved, which can consequently compensate the reduced curing depth due to the increased diffraction index of the nanoparticles. Therefore, much higher vertical resolution and better surface quality can be accomplished. (2) The vat depth is independent of the part height. Thus a shallow vat can be used to reduce the required volume of the liquid resin as well as the nanoparticles, allowing for testing of multiple nanomaterial concentration without the need of contamination and material waste. (3) Recoating is achieved by constraining the

resin between the previously cured layer and resin vat. Hence no additional sweeping is needed to flatten the surface, which in turn dramatically improves the fabrication speed. A typical pure polymer part and a graphene reinforced part built by this process are shown in figure 1(b).

Microstructure characterization

Transmission electron microscope (TEM) observations were carried out by a JEOL JEM 2100F TEM operated at 200 kV. The point-to-point resolution is 0.19 nm.

Mechanical property testing

The tensile and compression test were conducted on MTS 100 machine.

Results and discussion

Tensile test

To investigate the strengthening effect of GOs on a 3D printed component, we printed tensile test samples under different printing conditions. The tensile test results are shown in figure 2(a). Tensile strength of polymer is 8.939 MPa and the strength increased to 11.168 ± 0.565 MPa and 12.992 ± 0.656 MPa by integrating 0.2 wt.% and 0.5 wt.% GOs. The test results increased 24.9% and 45.3% by 0.2 wt.% and 0.5 wt.% of GOs, respectively. The tensile strain of 3D printed composites was 0.142 ± 0.008 and 0.170 ± 0.036 , which retained a good ductility when compared to the pure polymer (0.188). The 3D printed polymer and composites were heat treated in a furnace at 60 °C for 6 h and then increased to 110 °C for 6 another hours. The tensile strength of both were increased, which are 13.554 MPa and 14.497 MPa. The strain were also increased to 0.240 and 0.212, respectively. The strength of printed composites increased 62.2% and even the strain increased 12.8% from the printed polymer. The tensile test results had a great increase in

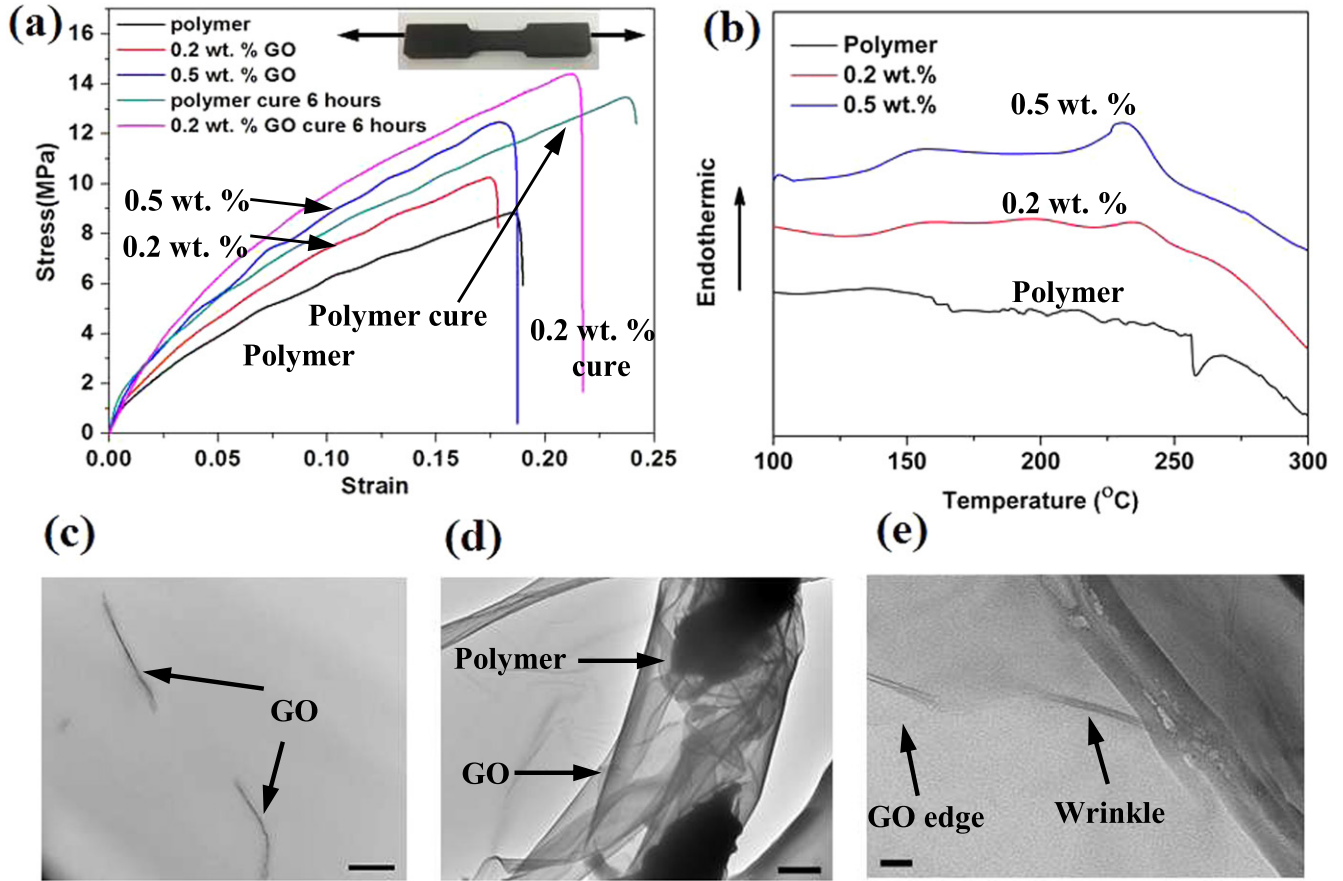


Figure 2. (a) Tensile test of 3D printed polymer and GO-reinforced tensile samples, (b) DSC for 3D printed nanocomposites as a function of GO weight fraction. TEM image showing the distribution of GOs in polymer. (c) GOs perpendicular to the TEM sample, scale bar: 1 μm . GOs in plane: (d) at the edge of the TEM sample, scale bar: 1 μm , (e) at the middle of TEM sample, scale bar: 5 nm.

both strength and ductility, showing the 3D GO-reinforced structure have better mechanical performance than pure polymer structures.

Strengthening mechanism

We studied the strengthening mechanism of GO-composites.

The force, F_B , required for the failure of GO nanocomposites can be expressed as [44]:

$$F_B = \sigma_P A_{\text{bulk}} + \sigma_{\text{shear}} A_{\text{interface}} = \sigma_C A, \quad (1)$$

where σ_P is the matrix tensile strength, A_{bulk} is the area of the bulk component of the fracture surface, σ_{shear} is the polymer shear strength and $A_{\text{interface}}$ is the area of the interface component of the fracture surface. In addition, σ_C is the nanocomposite tensile strength and A is the cross sectional area of the substrate.

The volume fraction of GOs can be written as:

$$V_f = \frac{V_{\text{GO}}}{V} = \frac{N\pi r_{\text{GO}}^2 h}{V}, \quad (2)$$

where V_{GO} is the total volume of GO, N is the total number of GO, r_{GO} is the average radius of GO, h is the thickness of GO and V is the total volume of the nanocomposites.

Each GO sheet can be considered as occupying a certain volume of the nanocomposite, this volume per GO, $V_{\text{GO}-M}$

can be found by re-arranging equation (3):

$$V_{\text{GO}-M} = \frac{V}{N} = \frac{\pi r_{\text{GO}}^2 h}{V_f}. \quad (3)$$

If we model the volume per GO as a cubic solid with the height of $2r_{\text{GO}}$ (z direction) and the values at x, y direction are considered as a when we assume the GOs are randomly aligned in the cross section of the rectangular solid, we have:

$$V_{\text{GO}-M} = 2a^2 r_{\text{GO}}. \quad (4)$$

Combining equations (3) and (4):

$$a = \sqrt{\frac{\pi r_{\text{GO}} h}{2V_f}}. \quad (5)$$

We can assume we have n GOs in the cross section, and n is given by:

$$n = \frac{A}{a^2} = \frac{2AV_f}{\pi r_{\text{GO}} h}. \quad (6)$$

If we cut the certain volume of nanocomposite at z direction randomly, we would cut the GO with a cross section

value from 0 to $2r_{GO}$. The average area of the cross section is $\pi r_{GO}/2$. The bulk component A_{bulk} , is given by the cross-section filled with metals:

$$A_{bulk} = A - n\pi r_{GO}(h + 2b)/2, \quad (7)$$

where b is the average thickness of the crystalline coating.

The interface area of all the GO protruding from the fracture surface is:

$$A_{interface} = n\frac{3}{16}\pi r_{GO}^2 \cos \theta \cos \alpha = n\frac{3}{64}\pi^2 r_{GO}^2, \quad (8)$$

where α and θ are the average angle of random GO at x and z direction, the average angle is 45° .

Combining equations (3), (8), (9), and (10), we have:

$$\sigma_C = \left[\sigma_{Shear} \frac{3\pi r_{GO}}{32} - \sigma_P(h + 2b) \right] \frac{V_f}{h} + \sigma_P. \quad (9)$$

Modification of Halpin–Tsai model

Several well-known models, e.g. Voigt [45] and Reuss [46] models, have been proposed based on rule of mixture ‘ROM’ and used to evaluate the properties of composites. Later on, there are several semi-empirical models have emerged to correct the ROM model where correcting factors are introduced, including the modified rule of mixture, the Halpin–Tsai model [47] and Chamis model [48]. The Halpin–Tsai equations are based upon the ‘self-consistent micromechanics method’ developed by Hill [49]. It has been widely used in calculation of composites with various types of reinforcing phases. It is suitable for semicrystalline polymer matrix composites, by 3D printing in this work, in that the model assumes constructing a material having isotropic mechanical properties from layers or plies of a material which has anisotropic mechanical properties. The modified Halpin–Tsai model for 2D graphene oxide enhanced polymer composite can be written as:

$$\frac{E_G}{E_M} = \frac{3}{8} \left[\frac{1 + (4r_{GO}/h)\eta_l V_{GO}}{1 - \eta_l V_{GO}} \right] + \frac{5}{8} \left[\frac{1 + 2\eta_t V_{GO}}{1 - \eta_t V_{GO}} \right], \quad (10)$$

$$\eta_l = \frac{E_{GO}/E_M - 1}{E_{GO}/E_M + 4r_{GO}/h},$$

$$\eta_t = \frac{E_{GO}/E_M - 1}{E_{GO}/E_M + 2},$$

where E_G , E_{GO} and E_M are the tensile Young’s modulus of the composite, GO and matrix, respectively. The Young’s modulus of the polymer measured by experiment is 50.8 MPa. Suk *et al* found that the Young’s modulus of GO is layer number related [50]. The Young’s modulus of monolayer, two layer and three layer GO membranes are 207.6 ± 23.4 , 444.8 ± 25.3 , and 665.5 ± 34.6 GPa [50].

Differential scanning calorimetry (DSC)

DSC was conducted in order to measure the morphological properties of 3D printed composites. Figure 1(b) shows a melting peak of polymer in the region of 250°C – 270°C . It is needed to notice that the crystallization of pure polymer is around zero. The crystallinity peaks, appearing with increasing the weight ratio of GO, suggest that each GO has a crystalline coating, which agrees with previous reports [44]. The GO-nucleated coating can be assumed to be a sandwich coating, assuming GO is circular with certain thickness. The composite crystallinity, χ , can be written as a function of the number, M , of GO in the composite:

$$\chi = \frac{V_0}{V} + \frac{M[\pi(h + 2b)r_{GO}^2 - \pi hr_{GO}^2]}{V}, \quad (11)$$

where V_0 is the volume of crystalline regions not associated with GOs, r_{GO} is the average radius of GO, h is the thickness of graphene oxide, V is the total volume of nanocomposites. The total volume of GOs is defined by:

$$V_{GO} = M\pi r_{GO}^2 h. \quad (12)$$

Combining equations (11) and (12), we have:

$$\chi = \frac{V_0}{V} + \frac{2b}{h} \frac{V_{GO}}{V}. \quad (13)$$

The slope in equation (13) can be fitted to the data of crystallinity and gives a value b/h of 56.87, where h is, provided by the manufacturer, 0.95 ± 0.25 nm. The average value of b is 54 ± 14.2 nm. The crystallinity propagates a large distance from the GO surface, which means that the GOs interact with crystalline polymer surface. In the other turns, it also means the crystalline coated GOs are embedded in the polymer. The total polymer-GO binding energy can be maximized by this virtually complete polymer coating [51]. This will be beneficial for the interfacial load transfer [52]. The generated crystalline explains the high ductility performance of 3D printed GO nanocomposites.

Cross-sectional microstructure

TEM was used to characterize the internal microstructure, especially the GO distribution in polymer, of the 3D printed nanocomposites. Figure 2(c) shows GOs are vertically distributed in the cross section. Figure 2(d) shows wrinkled GO on the edge of TEM sample, where the dark part is marked as the polymer matrix. Figure 2(e) shows GO lies in the plane of TEM sample. The GO is not fully flat in the cross section of TEM sample, which has a thickness around 100 nm, so that we can observe its edge and cross section of wrinkled part cut of the TEM sample. Based on the observation of TEM images, GOs were randomly distributed in the polymer matrix, including both in-plane, and normal to TEM sample.

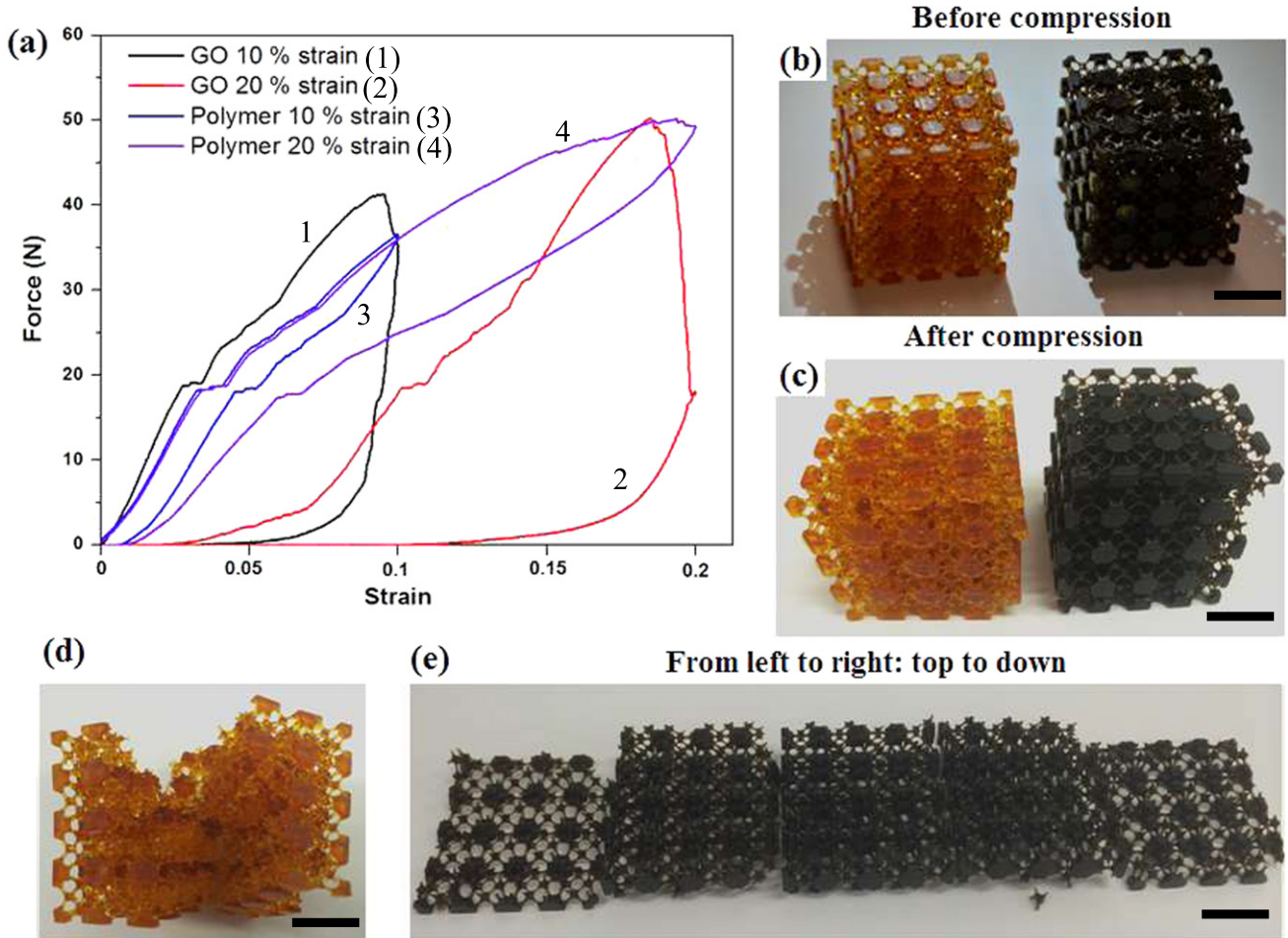


Figure 3. Compression test of 3D printed polymer and GO reinforced parts. (a) Force and strain curves. (b) 3D parts before compression test, scale bar: 20 mm. (c) 3D parts after compression, scale bar: 20 mm. (d) Interior deformation after compression, scale bar: 20 mm. (e) GO reinforced 3D parts delaminated as layers, top to bottom layers are from left to right, scale bar: 20 mm.

Mechanical behavior of 3D stereolithography printed complex structures

We also investigated the mechanical performance of various 3D GO-reinforced structures. The 3D GO structures shown in figure 3 are fabricated by SLA process with 0.5 wt.% of GOs. In order to quantify the mechanical behaviors, we subjected both the polymer and GO filled 3D components with different designs to in-plane compression test. The initial printed parts are shown in figure 3(b) and the structures after compression test is shown in figure 3(c). The videos of the compression of the 3D structure with and without GO fillings are demonstrated in the supporting materials. Representative force-strain curves are shown in figure 3(a). It needs more force to compress GO filled parts in order to achieve 10% of strain. The strengthening effect was caused by the stress concentration around GO and between them [53, 54]. The strain between nanofillers can be around 200% of strain when compared without nanofillers [53]. We conducted compression tests with 20% strain which provide more interesting information. GO-filled parts achieved the highest compressive force before reaching 20% of strain. During the compression test, the major failure modes of polymer parts are elastic wall

buckling, node rotation and tensile failure. The 3D GO structure was broken into five sections, which are shown in figure 3(e). It is due to shear stress developed during compression in the truss structure and the stress concentration around the GO nanofiller and polymer crystal.

In order to further investigate the mechanical behavior of GO-filled parts, a triangular honeycomb shape structure was built up by the same 3D printing process. The scaling laws governing the elastic modulus and strength of cellular materials are well established [55]:

$$\frac{E}{E_s} = B \left(\frac{\rho}{\rho_s} \right)^b \quad (14)$$

and

$$\frac{\sigma_c}{\sigma_{TS}} = C \left(\frac{\rho}{\rho_s} \right)^c, \quad (15)$$

where E_s , σ_{TS} and ρ_s are the Young's modulus, tensile strength, and density of the base solid material, respectively, E and σ_c are the Young's modulus and strength, respectively. For printed triangular shape, $B = C = 1/3$ and $b = 1$. The exponent c depends on the nature of failure in the material,

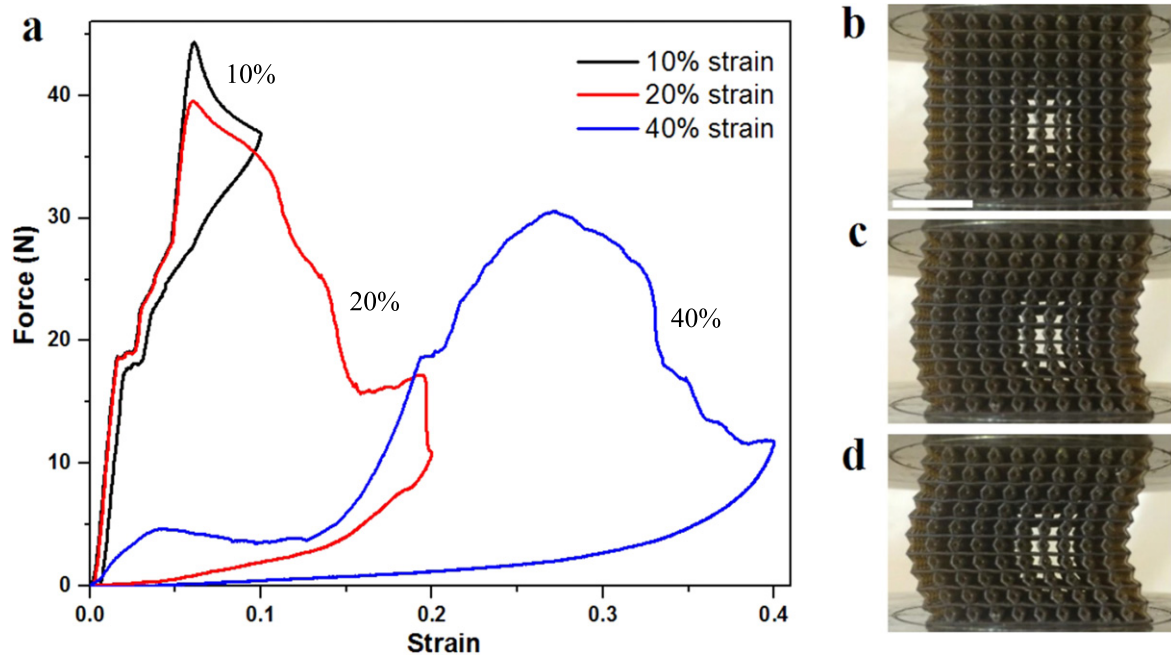


Figure 4. Compression test of 3D printed GO reinforced truss structure. (a) Force and strain curves at various strains. (b) Initial truss structure, scale bar: 10 mm. (c) Truss deformation at 5% of strain. (d) Truss deformation at 10% of strain.

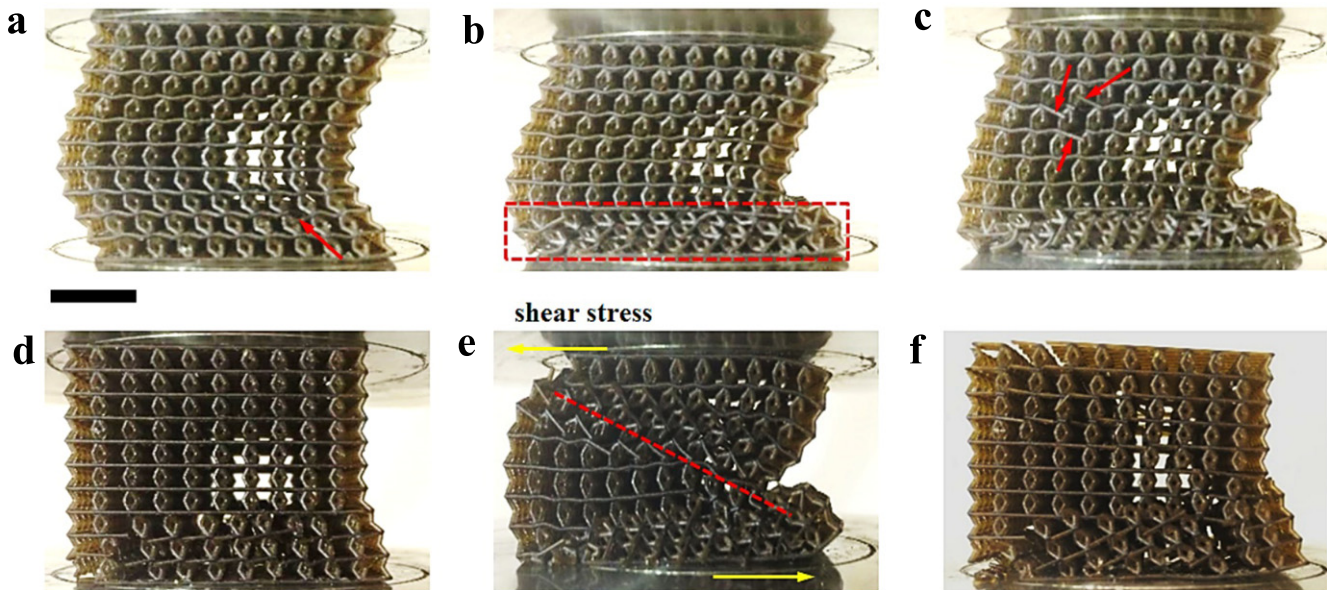


Figure 5. Various failures in GOs truss structure under compression with time sequence. (a) First failure at the truss node. (b) Truss deformation concentrated in the bottom two layers. (c) Further failure at some other truss node. (d) After relief of 20% compression, truss structure partially recovered. (e) Shear band generated by the shear force for 40% of compression. (f) After relief of 40% compression. Scale bar: 10 mm.

$c = 1$ when the cell walls fail in uniaxial tension or compression, and $c = 2$ when the cell walls fail via elastic buckling. The mechanical behavior of such structures depends on the properties of base material, architecture and relative density [56].

The force-strain curve, with 10%, 20% and 40% strain, of GO reinforced 3D structure is shown in figure 4(a). The whole test process is shown in supporting video 1 and supporting video 2. Figures 4(b)–(d) shows the initial truss

structure, 5% compression and 10% compression, respectively. The buckling deflection, as shown in figure 4(b), is the major deformation when under compression to 10% strain. After the compression test with 10% strain, we further conducted compression test with 20% strain. The node rotation failure, which is shown in figure 5(a), was firstly happened beyond the strain of 10%. For the whole truss structure, the stress concentration was located at the node. From the microstructure side, the stress was concentrated around the

nanofillers. The failure caused by the stress concentration at micro and macro level firstly occurred at the node. After that, the major failure only existed in the bottom two layers, which is the biggest difference when compared to the compression responses of pure polymer structure. GOs were randomly distributed in the cross section of 3D truss structures. There is a chance for one or few layers (randomly decided) that have larger stress concentration and then the stress was concentrated on that layer. The stress concentration caused the failure of the bottom two layers. During further compression, some more node failure occurred, as shown in figure 5(c). After removing the applied force, the truss structure recovered except the bottom two layers, which is shown in figure 5(d). The truss structure was then compressed to 40%, a metal like shear strain was shown in figure 5(e). There is a slip plane, similar to those in crystalline metal materials, in the GO-integrated truss structure, but not appearing in the non-GO reinforced composites. The shear stress at both sides of the truss structure caused the slip plane in the truss structure. After relief of the compression from 40% strain, we can see in figure 5(f) that the truss structure was fully destroyed.

Conclusion

In summary, we have demonstrated the first stereolithography printed 3D graphene oxide structures with good mechanical properties, especially with improvement in both strength and ductility. With only 0.2% GOs, the tensile strength is increased by 62.2% and elongation increased by 12.8%. TEM results show that the GOs were randomly aligned in the cross section of polymer. We investigated the strengthening mechanism of the 3D printed graphene oxide structures in terms of tensile strength and Young's modulus. DSC was also utilized to study the changes in crystallinity of GOs polymer composites, which is the reason behind the high ductility of the 3D printed nanocomposites. Compression test of 3D GOs polymer composites reveals the failure model of GOs truss structures.

References

- [1] Ramanathan T *et al* 2008 Functionalized graphene sheets for polymer nanocomposites *Nat. Nanotechnology* **3** 327–31
- [2] Print me a Stradivarius: how a new manufacturing technology will change the world *The Economist* (17 February 2011) p 7
- [3] Bourell D, Beaman J, Leu M C and Rosen D 2009 A brief history of additive manufacturing and the roadmap for additive manufacturing: looking back and looking ahead *US-Turkey Workshop on Rapid Technologies*
- [4] Gibson I, Rosen D W and Stucker B 2010 *Additive Manufacturing Technologies* (Berlin: Springer)
- [5] Lin D *et al* 2014 Three-dimensional printing of complex structures: man made or toward Nature? *ACS Nano* **8** 9710–5
- [6] Lee C, Wei X, Kysar J W and Hone J 2008 Measurement of the elastic properties and intrinsic strength of monolayer graphene *Science* **321** 385–8
- [7] Terrones M *et al* 2011 Interphases in graphene polymer-based nanocomposites: achievements and challenges *Adv. Mater.* **23** 5302–10
- [8] Lin D 2013 A laser sintered layer of metal matrix consisting of 0D, 1D and 2D nanomaterials and its mechanical behaviors *PhD Thesis* Purdue University
- [9] Fang M, Wang K, Lu H, Yang Y and Nutt S 2009 Covalent polymer functionalization of graphene nanosheets and mechanical properties of composites *J. Mater. Chem.* **19** 7098–105
- [10] Rafiee M A *et al* 2010 Fracture and fatigue in graphene nanocomposites *Small* **6** 179–83
- [11] Gong L, Young R J, Kinloch I A, Riaz I, Jalil R and Novoselov K S 2012 Optimizing the reinforcement of polymer-based nanocomposites by graphene *ACS Nano* **6** 2086–95
- [12] Young R J, Gong L, Kinloch I A, Riaz I, Jalil R and Novoselov K S 2011 Strain mapping in a graphene monolayer nanocomposite *ACS Nano* **5** 3079–84
- [13] Zhao X, Zhang Q, Chen D and Lu P 2010 Enhanced mechanical properties of graphene-based poly(vinyl alcohol) composites *Macromolecules* **43** 2357–63
- [14] Rafiee M A, Rafiee J, Wang Z, Song H, Yu Z-Z and Koratkar N 2009 Enhanced mechanical properties of nanocomposites at low graphene content *ACS Nano* **3** 3884–90
- [15] Xu Z and Gao C 2010 *In situ* polymerization approach to graphene-reinforced nylon-6 composites *Macromolecules* **43** 6716–23
- [16] Lin D, Richard Liu C and Cheng G J 2014 Laser sintering of separated and uniformly distributed multiwall carbon nanotubes integrated iron nanocomposites *J. Appl. Phys.* **115** 113513
- [17] Lin D, Richard Liu C and Cheng G J 2014 Single-layer graphene oxide reinforced metal matrix composites by laser sintering: microstructure and mechanical property enhancement *Acta Mater.* **80** 183–93
- [18] Stankovich S *et al* 2006 Graphene-based composite materials *Nature* **442** 282–6
- [19] Hicks J, Behnam A and Ural A 2009 A computational study of tunneling-percolation electrical transport in graphene-based nanocomposites *Appl. Phys. Lett.* **95** 213103
- [20] Zhang H-B *et al* 2010 Electrically conductive polyethylene terephthalate/graphene nanocomposites prepared by melt compounding *Polymer* **51** 1191–6
- [21] Chu K, Li W-S, Jia C-C and Tang F-L 2012 Thermal conductivity of composites with hybrid carbon nanotubes and graphene nanoplatelets *Appl. Phys. Lett.* **101** 211903
- [22] Yang S-Y *et al* 2011 Synergetic effects of graphene platelets and carbon nanotubes on the mechanical and thermal properties of epoxy composites *Carbon* **49** 793–803
- [23] An X, Butler T W, Washington M, Nayak S K and Kar S 2011 Optical and sensing properties of 1-pyrenecarboxylic acid-functionalized graphene films laminated on polydimethylsiloxane membranes *ACS Nano* **5** 1003–11
- [24] Xu Y *et al* 2009 A graphene hybrid material covalently functionalized with porphyrin: synthesis and optical limiting property *Adv. Mater.* **21** 1275–9
- [25] Liang J *et al* 2009 Electromagnetic interference shielding of graphene/epoxy composites *Carbon* **47** 922–5
- [26] Zhang H-B, Yan Q, Zheng W-G, He Z and Yu Z-Z 2011 Tough graphene-polymer microcellular foams for electromagnetic interference shielding *ACS Appl. Mater. Interfaces* **3** 918–24
- [27] Bunch J S *et al* 2008 Impermeable atomic membranes from graphene sheets *Nano Lett.* **8** 2458–62
- [28] Compton O C, Kim S, Pierre C, Torkelson J M and Nguyen S T 2010 Crumpled graphene nanosheets as highly effective barrier property enhancers *Adv. Mater.* **22** 4759–63

- [29] Kim H, Miura Y and Macosko C W 2010 Graphene/polyurethane nanocomposites for improved gas barrier and electrical conductivity *Chem. Mater.* **22** 3441–50
- [30] Kuilla T, Bhadra S, Yao D, Kim N H, Bose S and Lee J H 2010 Recent advances in graphene based polymer composites *Prog. Polym. Sci.* **35** 1350–75
- [31] Lin D, Ye C, Liao Y, Suslov S, Liu R and Cheng G J 2013 Mechanism of fatigue performance enhancement in a laser sintered superhard nanoparticles reinforced nanocomposite followed by laser shock peening *J. Appl. Phys.* **113** 133509
- [32] Verdejo R, Bernal M M, Romasanta L J and Lopez-Manchado M A 2011 Graphene filled polymer nanocomposites *J. Mater. Chem.* **21** 3301–10
- [33] Lee W D and Im S S 2007 Thermomechanical properties and crystallization behavior of layered double hydroxide/poly(ethylene terephthalate) nanocomposites prepared by *in-situ* polymerization *J. Polymer Sci. B* **45** 28–40
- [34] Leroux F and Besse J-P 2001 Polymer interleaved layered double hydroxide: a new emerging class of nanocomposites *Chem. Mater.* **13** 3507–15
- [35] Sinha R S and Okamoto M 2003 Polymer/layered silicate nanocomposites: a review from preparation to processing *Prog. Polym. Sci.* **28** 1539–641
- [36] Lee J-H, Kim S K and Kim N H 2006 Effects of the addition of multi-walled carbon nanotubes on the positive temperature coefficient characteristics of carbon-black-filled high-density polyethylene nanocomposites *Scr. Mater.* **55** 1119–22
- [37] Kalaitzidou K, Fukushima H and Drzal L T 2007 A new compounding method for exfoliated graphite–polypropylene nanocomposites with enhanced flexural properties and lower percolation threshold *Compos. Sci. Technol.* **67** 2045–51
- [38] Wang W-P and Pan C-Y 2004 Preparation and characterization of polystyrene/graphite composite prepared by cationic grafting polymerization *Polymer* **45** 3987–95
- [39] Yavari F, Rafiee M A, Rafiee J, Yu Z Z and Koratkar N 2010 Dramatic increase in fatigue life in hierarchical graphene composites *ACS Appl. Mater. Interfaces* **2** 2738–43
- [40] Hector S J and Wicker R B 2006 Functionalizing stereolithography resins: effects of dispersed multi-walled carbon nanotubes on physical properties *Rapid Prototyping J.* **12** 292–303
- [41] Sandoval J H, Soto K F, Murr L E and Wicker R B 2007 Nanotailoring photocrosslinkable epoxy resins with multi-walled carbon nanotubes for stereolithography layered manufacturing *J. Mater. Sci.* **42** 156–65
- [42] Sun C, Fang N, Wu D M and Zhang X 2005 Projection micro-stereolithography using digital micro-mirror dynamic mask *Sensors Actuators A* **121** 113–20
- [43] Zhou C, Chen Y, Yang Z and Khoshnevis B 2011 Development of multi-material mask-image-projection-based stereolithography for the fabrication of digital materials *Annual Solid Freeform Fabrication Symp. (Austin, TX)*
- [44] Coleman J N et al 2004 High performance nanotube-reinforced plastics: understanding the mechanism of strength increase *Adv. Funct. Mater.* **14** 791–8
- [45] Darya Z S and Lvov G I 2015 The calculation of effective elastic constants in a composite with 3D orthogonal nonwoven fibers. Вестник Томского государственного университета Математика и механика
- [46] Reuss A 1929 Berechnung der Fließgrenze von Mischkristallen auf Grund der Plastizitätsbedingung für Einkristalle *ZAMM —J. Appl. Math. Mech. / Z. Angew. Math. Mech.* **9** 49–58
- [47] Affdl J C H and Kardos J L 1976 The Halpin–Tsai equations: a review *Polym. Eng. Sci.* **16** 344–52
- [48] Chamis C C 1989 Mechanics of composite materials: past, present, and future *J. Compos. Technol. Res. ASTM* **11** 3–14
- [49] Hill R 1964 Theory of mechanical properties of fibre-strengthened materials: I. Elastic behaviour *J. Mech. Phys. Solids* **12** 199–212
- [50] Suk J W, Piner R D, An J and Ruoff R S 2010 Mechanical properties of monolayer graphene oxide *ACS Nano* **4** 6557–64
- [51] Coleman J N and Ferreira M S 2004 Geometric constraints in the growth of nanotube-templated polymer monolayers *Appl. Phys. Lett.* **84** 798–800
- [52] Dalton A B et al 2003 Super-tough carbon-nanotube fibres *Nature* **423** 703
- [53] Akutagawa K, Yamaguchi K, Yamamoto A, Heguri H, Jinnai H and Shinbori Y 2008 Mesoscopic mechanical analysis of filled elastomer with 3d-finite element analysis and transmission electron microtomography *Rubber Chem. Technol.* **81** 182–9
- [54] Kishimoto H et al 2013 Visualization of nanoscale deformation in polymer composites with zernike-type phase-contrast x-ray microscopy and the finite element method *Polym. J.* **45** 64–9
- [55] Fleck N A, Deshpande V S and Ashby M F 2010 Micro-architected materials: past, present and future *Proc. R. Society A* **466** 2495–516
- [56] Compton B G and Lewis J A 2014 3D-printing of lightweight cellular composites *Adv. Mater.* **26** 5930–5